Impact of Monolayer WS_2 Surface Properties on the Gate Dielectrics Formation by Atomic Layer Deposition

Running title: Effect of WS_2 Surface on ALD dielectrics

Running Authors: Lin et al.

Zaoyang Lin,[†,‡,§,*] Sven Dekelver,[†,‡,§] Daire Cott,[‡] Benjamin Groven,[‡] Stefanie Sergeant,[‡] Thierry Conard,[‡] Xiangyu Wu,[‡] Pierre Morin,[‡] Dennis Lin,[‡] Cesar Javier Lockhart de la Rosa,[‡] Gouri Sankar Kar,[‡] and Annelies Delabie[‡,†,*]

[†] Department of Chemistry, KU Leuven, Celestijnenlaan 200F, Leuven, 3001, Belgium
[‡] imec, Kapeldreef 75, Leuven, 3001, Belgium
[§] Both authors contributed equally to this work.

[*] Electronic mail: Zaoyang.Lin@imec.be; Annelies.Delabie@imec.be

Two-dimensional transition metal dichalcogenides (2D TMDs), such as MoS_2 and WS_2, have emerged as promising channel materials for future generation transistors. However, carbon-based surface contaminants pose a significant challenge in the formation of high-quality metal-oxide-semiconductor (MOS) gate stacks for 2D TMDs. Carbon-based surface contaminants are known to be present even on directly grown 2D TMDs that have not been in contact with polymers. These organic contaminants affect precursor adsorption during atomic layer deposition (ALD) of gate dielectrics on 2D TMDs and as such the 2D-dielectric interface. This study examines the effectiveness of pre-deposition annealing in mitigating carbon-based contaminants while maintaining the integrity of a directly grown WS_2 monolayer on a SiO_2 substrate. We show that a WS_2 monolayer on a SiO_2/Si substrate remains stable during vacuum anneal at temperatures up to 400°C. Water contact angle (WCA) measurements and X-ray photoelectron spectroscopy (XPS) confirm that the surface concentration of carbon starts to decrease at 150°C. Thermal anneal improves the

surface coverage of Al_2O_3 for both conventional chemisorption-based ALD and physisorbed-precursor-assisted (PPA) ALD processes by facilitating more effective Al_2O_3 nucleation on the WS_2 monolayer. The impact of pre-deposition anneal on the Al_2O_3 growth behavior in both processes can be explained by changes in surface contaminant levels. Our results underscore the importance of surface pretreatment in dielectric deposition on 2D TMDs and demonstrate that pre-deposition anneal is an effective method to enhance ALD-based dielectric deposition on directly grown 2D TMDs.

I. INTRODUCTION

Two-dimensional transition metal dichalcogenides (2D TMDs), such as MoS_2, WS_2, and WSe_2, are promising candidates for channel material in future generations of field-effect-transistors (FETs). They can maintain high mobility even at monolayer thickness, enabling a better electrostatic control than silicon at ultra-short FET gate length[1,2].

The surface cleanliness of 2D TMDs is essential for both gate stack and contact formation. In silicon gate stack technology, the superior Si-SiO_2 interface can be formed by re-oxidation[3]. However, applying similar methodology on 2D TMDs is challenging due to their monolayer nature. Therefore, carbon-based residues and airborne organic contaminants introduced by different integration schemes on the surface of 2D TMDs should be well understood.

One prevalent method of integrating high-quality 2D TMDs involves a transfer process[4]. In this approach, 2D TMDs are grown on a template substrate designed to facilitate van der Waals epitaxial growth, which are subsequently transferred from the

template substrate to the target substrate, commonly using a sacrificial polymer adhesion layer. While this approach provides the best device performance in lab vehicles[5,6], the removal of the polymer adhesive layer (such as Polymethyl methacrylate (PMMA)[7,8]) used in the bonding process can leave carbon residues on 2D TMD surface upon removal[9]. Although these transfer residues are sometimes considered to facilitate the Atomic Layer Deposition (ALD) nucleation on the basal planes of the 2D TMDs[10,11], they can introduce non-uniformity and impurities at the semiconductor-dielectric interface, which can be detrimental to the carrier transport and reliability of FETs. Significant active research focusses on removing the organic contamination induced from transfer, either by improving the transfer process itself (e.g., metal-assisted transfer[12] and UV release tape[13]) or by enhancing post transfer cleaning steps (e.g., plasma cleaning of the transfer residual[14]).

Another promising integration strategy is to grow 2D TMDs directly on the target substrates (which can be either bottom gate dielectrics or sacrificial layers). It has been demonstrated that monolayer 2D TMDs can be grown at wafer scale on SiO_2/Si substrates[15,16]. This approach can eliminate the need for a transfer step, making it attractive from an integration point of view. However, the best mobility achieved for directly grown 2D TMDs on amorphous substrates[17,18] is substantially lower than the best values obtained for epitaxially grown 2D TMDs. Extensive research efforts therefore focus on improving the structure and material quality of directly grown 2D TMDs on amorphous substrates[19]. In addition, the surface organic contamination remains a challenge even for the direct-growth integration strategy. Time-of-flight secondary ion mass spectrometry (TOF-SIMS) measurements have confirmed the presence of organic

adlayers formed by airborne carbon-based contamination on the surface of direct-growth MoS_2[20]. The contamination from the airborne species can also be a concern for transferred 2D TMDs after cleaning.

Studies have reported that thermal anneal can reduce the carbon concentration and improve the surface coverage of ALD grown dielectrics on MoS_2[21]. It is also a common method to remove transfer residual and airborne contamination on graphene[22]. As low-temperature processing is generally considered as a requirement for 2D TMD FETs[23], the thermal budget introduced in the annealing can be a concern for the integrity of the devices. However, these thermal constrains are primarily determined by integration choice and process flows, rather than inherent material limitations. For instance, some metal contacts (e.g., Bi, Sn) for 2D TMDs cannot withstand high temperature[24]. These challenges can be partially addressed by adapting the process flow. For example, a gate-first integration can circumvent the impact of surface cleaning to the contact. On the other hand, the thermal stability of 2D TMDs presents an intrinsic limitation, which is largely dependent on the material quality and surrounding environment. Therefore, it is important to understand the thermal stability and assess the temperature limit for the pre-deposition anneal of 2D TMDs in a condition relevant to the integration.

Depositing nm-thin continuous dielectrics on 2D TMDs is challenging due to their self-passivated basal planes.[25,26] Conventional ALD is used to deposit high-κ gate dielectric in silicon technology. However, that tends to grow only on the defect sites of 2D materials. As a result, several techniques have been developed to enable the deposition of dielectrics on 2D materials, such as seeding layer evaporation[27,28], UV-O_3 treatment[29], and 2D dielectric stacking[30,31]. Low-temperature physisorbed-precursor-

assisted (PPA)-ALD is also considered promising for achieving conformal dielectric deposition, even on gate-all-around (GAA) structure[32]. Studies have shown that 2D TMDs become more hydrophobic after adsorbing airborne contaminants[33,34]. Precursor adsorption in ALD-based processes is closely related to surface energy and, consequently the water contact angle[35,36]. Therefore, we expect that removing organic contaminants can improve the surface coverage of dielectrics grown by ALD-based processes.

In this work, we systematically investigate the impact of thermal anneal on the surface properties of a directly grown WS_2 monolayer deposited by high-temperature metal-organic chemical vapor deposition (MOCVD) on a SiO_2/Si substrate. The effect of pre-deposition anneal on the ALD-based Al_2O_3 growth on a WS_2 monolayer is also studied and discussed based on the change of surface carbon-based contaminant. The study is based on complementary characterization techniques, including water contact angle (WCA) measurement, Raman spectroscopy, atomic force microscopy (AFM), and X-ray photoelectron spectroscopy (XPS).

II. EXPERIMENTAL

A. Preparation of monolayer WS_2

The WS_2 monolayers used in this study were grown by metal-organic chemical vapor deposition (MOCVD) on 12-inch Si wafers covered with 50 nm thermal SiO_2 obtained by dry oxidation. The growth process was performed at 950°C using H_2S and $W(CO)_6$ as precursors in an industry compatible reactor (Epsilon 3200, ASM)[37]. To ensure WS_2 coverage across the whole wafer, the MOCVD process was tuned to be

slightly overgrown. This resulted in some unintentionally grown second layers with triangular morphology and vertical crystals[38], as shown in Figure 1 (c). After removal from the growth chamber, the wafers were cleaved into coupons and stored in a dark cleanroom (CR) environment for at least 2 weeks to avoid photo-oxidation[39], serving as the reference of our study. Samples extracted immediately from the growth chamber are designated as "as-grown" in this study.

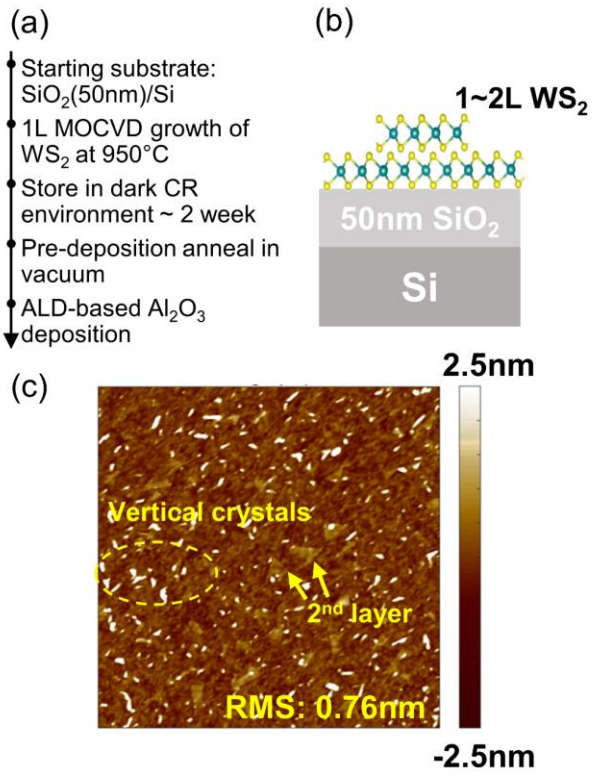

Figure 1. (a) Process flow; (b) Schematic of the sample structure; and (c) 1×1 μm^2 AFM surface topography of the WS_2 used in this study.

B. Thermal anneal setup

Thermal anneals were performed using a tube furnace and a rapid thermal anneal (RTA) system. The tube furnace was used to achieve better vacuum conditions (~ 4×10^{-3} mbar) for anneals at 1 hour. A maximum heating rate of 10°C/min was employed, followed by natural cooling. The RTA system was used to study the time-dependent characteristics for anneals less than 1 hour, as the target temperature could be reached within 30s. The pressure was set as 14 mbar during the RTA. For both tools, samples were removed after cooling below 80°C in vacuum. In subsequent sections, unless otherwise specified, thermal anneals conducted without specification correspond to a 1-hour anneal in the tube furnace, while others duration indicating RTA processing. We confirmed that both setups led to consistent results when annealing at the same temperature, as shown in the Results section.

C. Al_2O_3 dielectric deposition

In this study, we investigated two types of ALD-based Al_2O_3 deposition on a WS_2 monolayer: a standard chemisorption-based (conventional) ALD and a physisorbed-precursor-assisted (PPA)-ALD[32,40]. Trimethylaluminum (TMA) and H_2O were used as the precursors for aluminum and oxygen, respectively, in both processes. For the conventional ALD, the 300 mm chamber (PULSAR from ASM) was heated to 250°C. The TMA pulse/purge and H_2O pulse/purge times were set as 100/500 ms and 400/1600 ms, respectively. Both the water and TMA sources remained at ambient temperature. Note that the coupons were positioned on pocket wafers for processing in the 300mm reactor. For the PPA-ALD process, the coupons were exposed to ~ 10 Torr TMA partial pressure for 5 minutes. This was done in a different 300 mm ALD chamber (EMERALD, ASM). The reactor temperature was set at 100°C to minimize precursor desorption. The

TMA source was heated at 40°C to increase the vapor pressure. After TMA exposure, the chamber was pumped down, followed by a regular H_2O half-cycle. The pulse and purge times were set to 75 ms and 4000 ms, respectively. The Al_2O_3 depositions were performed within 1 hour after samples were removed from the vacuum anneal chamber.

D. Material characterization

Water contact angle (WCA) measurements were conducted using an OCAH230L contact angle tool from Dataphysics, with deionized water as the liquid phase. The water was dispensed by a 0.52 μm thick, 50 mm long needle attached to a Hamilton 500 μL syringe. The advancing WCA was measured by a camera setup and analyzed using the Laplace-Young method built in Dataphysics' SCA 20 software. By default, measurements were performed within 1 hour of sample removal from the vacuum chamber. At least 3 measurements were taken per sample at different positions to improve the statistical accuracy. The standard deviation for all measurements was lower than 2°.

Atomic force microscopy (AFM) images were acquired in PeakForce QNM® mode using an ICON PT Nanoscope V (Bruker) with an HQ:NSC19/Al BS probe under ambient conditions.

Raman measurements were performed using a Horiba Jobin-Yvon HR800 RAMAN tool with a 532 nm (~2mW) laser and 0.1% neutral density (ND) filter at room temperature. The exposure condition was fixed at 1×50 s. Three points were measured on each sample and the averages were used.

X-ray Photoelectron Spectroscopy (XPS) measurements were conducted in angle-integrated mode using a QUANTES instrument (Physical Electronics). The system

employed a monochromatized photon beam of 1486.6 eV (AlKα X-ray source) with a 100 μm spot size. This setup allows for a maximum penetration depth of ~ 8 nm, with most information is extracted 2~3 nm under the surface. Charge neutralization was used during measurements. Electrons were collected using a takeoff angle of 45°. The binding energy was calibrated by the adventitious C peak (284.8 eV).

III. RESULTS AND DISCUSSION

A. Impact of annealing on the surface properties of a WS_2 monolayer

First, we investigate the evolution of the surface energy of a WS_2 monolayer as a function of the annealing temperature. Water contact angle (WCA) measurements were conducted on a WS_2 monolayer annealed at temperatures ranging between 150ºC and 700ºC with a fixed anneal time of 1 hour. We compared these values to those of unannealed WS_2 reference samples. All WS_2 samples were stored for two weeks in a dark cleanroom environment prior to anneals and measurements. It should be noted that airborne molecular contaminants (AMCs) are still present in the cleanroom air[41]. Consequently, the WCA of reference samples reached a saturation WCA value of ~90°, presumably due to AMC adsorption during storage. This is in contrast to the WCA values of ~70° as obtained for as-grown WS_2.

For anneal temperatures up to 400°C, the WCA decreases from ~90° to ~65°, as shown in Figure 2 (a). The decrease in WCA already begins at 150°C, consistent with literature[42]. When the temperature increases from 400°C to 700°C, a sharp decrease in WCA is observed around 500°C, followed by a small increase at 700°C. These three regimes (RT~400°C, 400~500°C, and 500~700°C) can also be distinguished by surface

topography, as shown by the AFM images in Figure 3. The morphology of the WS_2 monolayer is well preserved for anneals up to 400°C, while clusters appear on the surface for anneals at 500°C and 700°C. Similarly, the characteristic Raman signals for the WS_2 monolayer[43] are well maintained for anneal temperatures up to 400°C but are lost for anneals at temperatures of 500°C and higher, as shown in Figure 2 (b). The decrease in WCA for annealing temperatures up to 400°C is likely attributed to the removal of surface contaminants from the WS_2 surface. This conclusion is supported by the preservation of WS_2 surface topography and structural properties in this temperature range.

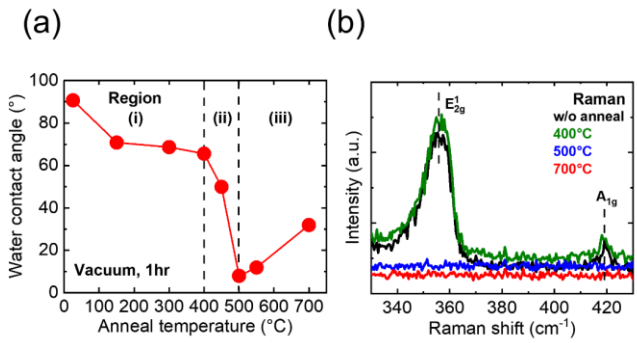

Figure 2. (a). Water contact angle (WCA) of WS_2 monolayer on SiO_2/Si substrate after 1-hour vacuum annealing at different temperatures. Three regions (room temperature ~ 400°C, 400°C ~ 500°C, and 500°C ~ 700°C) are identified based on the trend of WCA evolution. (b). Raman spectra of the WS_2 monolayer on a SiO_2/Si substrate after annealing at 400°C, 500°C, and 700°C.

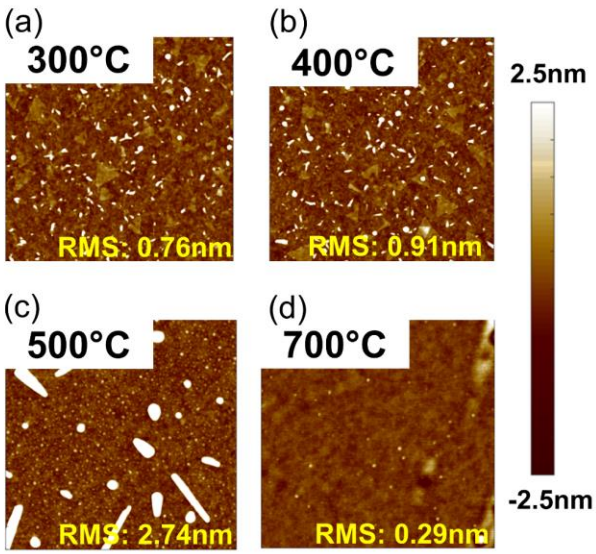

Figure 3. 1×1 μm^2 AFM images of the WS_2 monolayer measured after 1-hour vacuum annealing at (a) 300°C, (b) 400°C, (c) 500°C, and (d) 700°C.

In order to understand the surface chemical conditions of the three identified regions, we conducted X-ray photoelectron spectroscopy (XPS) analysis on the annealed WS_2 samples. Figure 4 presents the S 2p, W 4f, and O 1s XPS spectra for the WS_2 monolayer annealed at different temperatures. The chemical bonds in the WS_2 monolayer are well preserved during anneals at temperatures up to 400°C. The S/W ratio and nearly identical peak shapes for S 2p and W 4f before and after annealing (Figure 4 (a) and (b)) confirm this preservation. However, after annealing at 500°C, the S 2p signal disappears, indicating complete sulfur desorption from the surface. The W 4f doublet shifts to a higher binding energy (BE) with lower intensity, corresponding to WO_x formation. This observation aligns with the shoulder of the O 1s peak at lower BE seen at 500°C (Figure 4(c)). Three possible mechanisms have been proposed in literature to explain the

oxidation of 2D TMDs related to this work: (1) sulfur substitution by adsorbed oxygen, even on defect-free basal planes[44]; (2) oxygen chemisorption facilitated by sulfur vacancies[45]; and (3) SO_2 formation with adsorbed O_2 during annealing. It is reported that at 500°C the sulfur removal is due to SO_2 formation with remaining adsorbed O_2, and direct S desorption only occurs above 800°C for exfoliated MoS_2[46]. Therefore, the reaction of sulfur with adsorbed O_2 appears to be the most likely mechanism. However, both the material and growth conditions are different. We can therefore not rule out the possibility that direct S desorption already occurs during the 500°C anneal for the MOCVD-grown WS_2 monolayer, and that WO_x is formed when the sample is exposed to air. In-situ characterization would be necessary to confirm the exact mechanism. At 700°C, the W 4f signal also disappears, corresponding to the removal of WO_x and/or WS_2 from the surface. Stronger O 1s intensities are obtained for samples annealed at temperatures higher than 500°C compared to those annealed at lower temperatures. This observation can be attributed to the exposure of the SiO_2 substrate, consistent with the quenching of WS_2 Raman signals and the island-shaped structures observed in AFM results.

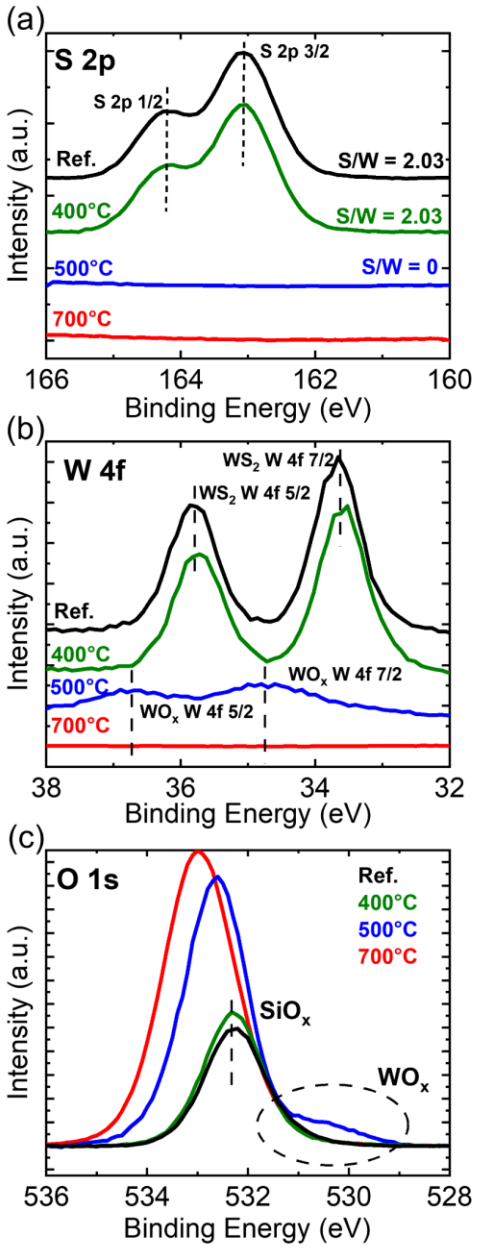

Figure 4. XPS spectra of (a) S 2p, (b) W 4f, and (c) O 1s for the WS_2 monolayer on a SiO_2 substrate after 1-hour vacuum annealing at 400°C, 500°C, and 700°C for 1 hour. The binding energy in (c) is aligned to emphasize the region corresponding to WO_x formation.

The effects of 1-hour vacuum annealing on the WS_2 material properties can be summarized as follows: (1) 150°C ~ 400°C: The WS_2 structure remains intact. The

observed decrease in water contact angle likely results from the removal of the organic adlayer; (2) above 400°C: sulfur completely desorbs from the surface, possibly due to direct desorption or reaction with adsorbed oxygen, leading to WO_x formation; (3) after reaching 700°C: both W and S desorb from the surface.

Next, we examine the impact of thermal anneal duration on the surface properties of the WS_2 monolayer. For the 300°C and 400°C anneals, the WCA stabilizes within one hour, to a value of ~73° at 300°C and ~64° at 400°C, as shown in Figure 5. The lower stabilized WCA for samples annealed at 400°C compared to 300°C suggests that some surface carbon-based contaminants may not be removed at 300°C. Additionally, the time required to reach a stable WCA is longer for annealing at 300°C compared to 400°C. The stabilized WCA values obtained by RTA are similar to the results obtained for anneals in a tube furnace. This suggests that the previously discussed WCA values for tube furnace anneals represents stabilized values at the respective temperatures. Furthermore, it indicates possible differences in the vacuum level of our experimental setups do not significantly affect the results.

For the 500°C anneal, a rapid WCA decrease occurs within 3-5 minutes, the WCA reaches the stabilized value at 400°C. Prolonged annealing at 500°C results in a strongly hydrophilic surface, consistent with the result of 1-hour tube furnace anneal. Due to WS_2 degradation at 500°C, a clear WCA stabilization region cannot be obtained, preventing confirmation of whether the WCA value achieved at 400°C represents a "clean" WS_2 surface.

The annealing ambient can also impact the thermal stability of the WS_2 monolayer. Although forming gas (95% N_2/5% H_2) annealing reportedly outperforms

vacuum annealing in improving dielectric coverage[21], our experiments at 400°C for 20 minutes yielded similar WCA values in forming gas (~ 68°) and vacuum (~ 64°). This suggests that at least for annealing below 400°C, the reducing atmosphere may not significantly alter WS_2 surface properties. Further investigation is needed to fully understand the role of annealing ambient in pre-deposition anneal and is outside the scope of this paper.

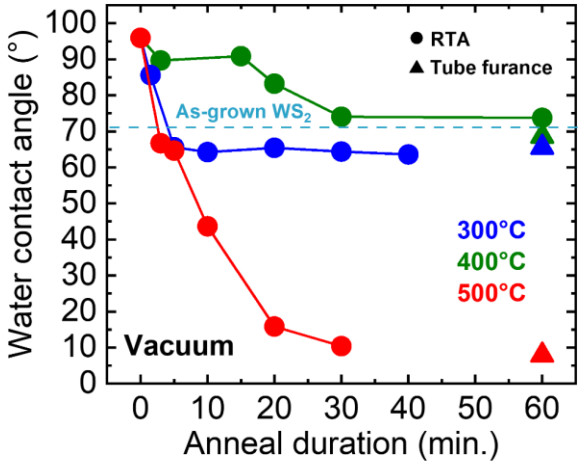

Figure 5. Water contact angle (WCA) of WS_2 monolayer/SiO_2 structures as a function of annealing duration and temperatures. WCA of as-grown WS_2 was measured within 15 minutes of sample retrieval from the growth chamber.

Since there is inevitably a delay between the thermal anneal and subsequent process, we investigated the evolution of WCA over time following sample retrieval from vacuum chambers. Samples were stored in a dark cleanroom environment during this interval. Figure 6 (a) shows that the post-annealing low WCA value of ~ 65° persists for only a few hours. Interestingly, as-grown WS_2 exhibits a higher WCA than WS_2 annealed at 400°C. The WCA increases to approximately 85° after one day and saturates at ~ 90° after two weeks, regardless of whether the WS_2 is as-grown or annealed. These results

underscore the importance of minimizing the delay between pre-deposition anneal and subsequent process to maximize the potential benefits.

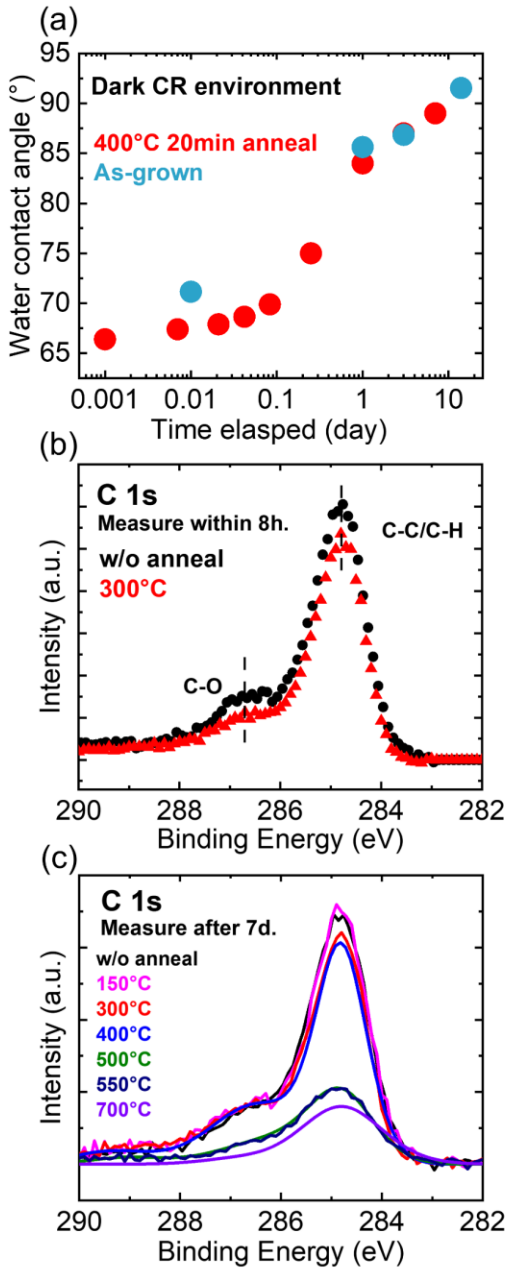

Figure 6. (a). Evolution of water contact angle (WCA) of a WS_2 monolayer on a SiO_2/Si substrate over time after sample retrieval from the vacuum chamber. As-grown WS_2 refers to samples freshly withdrawn from the growth chamber, whereas annealed samples were stored in dark cleanroom environments for at least two weeks prior to annealing.

(b). XPS C 1s spectra of the WS_2 monolayer on a SiO_2/Si substrate with and without 1-hour vacuum annealing at 300°C. Samples were transferred from the annealing chamber to the XPS chamber within 8 hours. Spectra are normalized to the Si 2p peak intensity. (c). XPS C 1s spectra of a WS_2 monolayer on a SiO_2/Si substrate after annealing at various temperatures. Samples were stored in a dark cleanroom environment for 7 days before loading for XPS. All WS_2 samples in (b) and (c) underwent 2-week cleanroom air exposure before any processes.

To chemically verify the removal of surface carbon, we compared XPS C 1s spectra of annealed samples, measured within 8 hours after annealing, to those of reference samples. Figure 6 (b) presents these results, normalized to the Si 2p peak intensity. 300°C annealed samples exhibited a reduction in the signal corresponding to C-C/C-H and C-O regions[47]. The adventitious carbon peak (~284.8 eV) is notably sensitive to the sample preparation. Nevertheless, the reduced intensity of the higher BE peak at ~ 286 eV corresponding to C-O bonds, evidences the partial removal of surface carbon by annealing. Figure 6 (c) displays XPS C 1s spectra measured after one week for samples annealed at various temperatures. Samples annealed at 300°C and 400°C still show a slight decrease in the C-C/C-H peak, while C-O peak remain similar for samples annealed below 500°C. This is consistent with the restoration of WCA after 7 days. Interestingly, the anneals at temperatures that damage the WS_2 monolayer result in a significant reduction in both the C-C/C-H and C-O peaks. This suggests that the WS_2 monolayer on the SiO_2/Si substrate has a higher affinity for airborne molecular contaminants adsorption compared to SiO_2 or WO_x surfaces. This observation aligns with the higher dispersive component of the surface energy of the WS_2 monolayer compared to bare SiO_2 substrate, as reported in literature[42]. More detailed experiments are still

necessary to quantify carbon levels before or at the initial stage (< 1 min) of WS_2 air exposure.

B. Impact of annealing on ALD-based Al_2O_3 deposition on a WS_2 monolayer

We investigated two different Al_2O_3 deposition processes to elucidate the impact of thermal anneal on ALD-based dielectric deposition. The first process is conventional chemisorption-based ALD, where TMA chemisorbs on the substrate through ligand exchange. Given the self-passivated nature of 2D TMD basal planes, Al_2O_3 nucleation is limited to grain boundaries and defect sites[48]. The second process is physisorbed-precursor-assisted (PPA)-ALD. This process enables Al_2O_3 nucleation on 2D TMD basal planes by TMA physisorption on 2D TMDs surface at low temperature and high precursor partial pressures[32]. We extracted height distributions from AFM images for both conventional ALD at 250°C and PPA-ALD at 100°C under various pre-anneal conditions. Figure 7 presents these results, including a 3-minute anneal at 500°C for PPA-ALD. While minor degradation of a WS_2 monolayer cannot be excluded, we propose that the WS_2 monolayer remains largely intact for this condition. This is supported by the WCA similarities with the 400°C anneal (Figure 5) and the comparable surface topography to the reference sample after PPA-ALD (Figure 7 (c)). Figure 7 (a) and (b) present the AFM height distribution after Al_2O_3 deposition on the WS_2 monolayer. The area of the peak at zero height indicates the percentage of WS_2 surface uncovered by Al_2O_3. The Al_2O_3 growth behavior can be characterized by the probability distribution of heights exceeding zero.

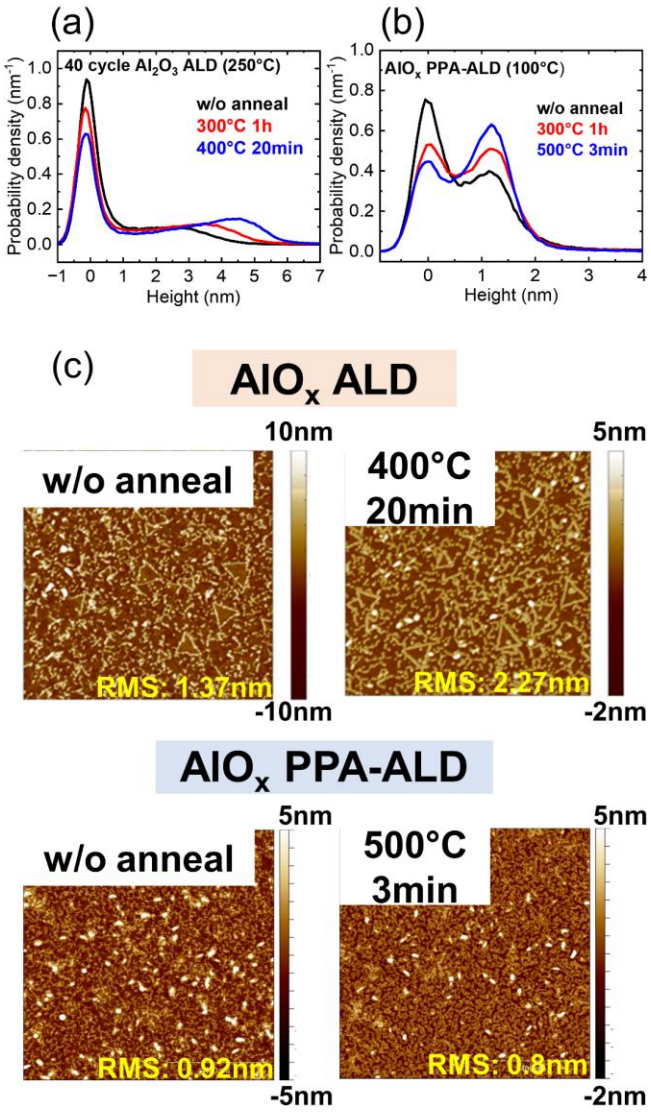

Figure 7. AFM height distribution extracted after (a) conventional 40 cycle Al_2O_3 ALD at 250°C and (b) physisorbed-precursor-assisted (PPA)-ALD AlO_x at 100°C on a WS_2 monolayer on a SiO_2/Si substrate with different pre-deposition anneal conditions. (c) 1×1 μm^2 surface topography of $AlO_x/WS_2/SiO_2/Si$ structures used for the extraction of the height distribution in (a), (b).

Both deposition methods exhibit improved surface coverage at elevated annealing temperatures, as evidenced by the diminished peak area at zero height in Figure 7 (a) and (b). Additionally, non-destructive anneals preserve the RMS surface roughness of the WS_2 monolayer within 1 ~ 2 Å (Figure 8 (a)). Therefore, the increased RMS surface

roughness obtained after 40 cycles of conventional AlO_x ALD is attributed to factors other than changes in the WS_2 surface morphology. In contrast, the RMS surface roughness of the WS_2 monolayer after AlO_x PPA-ALD is relatively unaffected by pre-deposition anneal. Moreover, with increasing anneal temperature, the AFM AlO_x thickness (Figure 8 (b)), defined as interpeak distance in AFM height distribution, rises for the 40-cycle conventional ALD but remains largely constant for the PPA-ALD process.

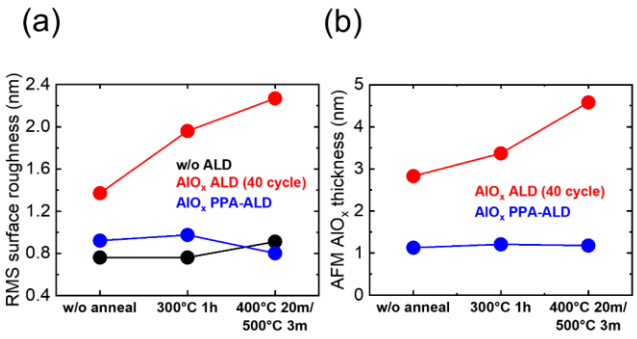

Figure 8. (a). RMS surface roughness and (b) AlO_x film thickness of a WS_2 monolayer under different anneal conditions and ALD-based processes extracted by the AFM images. AFM AlO_x thickness is defined as the interpeak distance in Figure 7 (a) and (b).

Figure 9 shows a model based on surface carbon-based contaminant changes that consistently explains the above observations. During conventional ALD, TMA adsorption is limited to chemisorption on defect sites. The broader AlO_x height distribution may result from the gradual removal of surface contaminants during deposition, as 250°C chamber temperature is sufficient to desorb them from the WS_2 monolayer surface. Contaminant removal activates new nucleation sites during the ALD process. This results in a broader height distribution[49], as Al_2O_3 nuclei are being generated continuously during ALD. The increase of AlO_x thickness with elevated

annealing temperature likely results from more thorough surface contaminant removal at defect sites, facilitating the initiation of nucleation sites earlier during the ALD process. The height increase may also be related to enhanced TMA surface diffusion on the basal plane after surface contaminant removal, promoting aggregation and nucleation at defect sites and island growth. The combined effects of height distribution broadening and increased AlO_x thickness account for the elevated RMS surface roughness observed at higher annealing temperatures in the chemisorption ALD process.

In contrast, PPA-ALD facilitates TMA adsorption on both basal planes and defect sites. Without pre-deposition anneal, surface contaminants likely persist during the growth process, as the reactor temperature (100°C) set to promote physisorption is insufficient for contaminant removal. After pre-deposition anneal, a larger fraction of the basal plane is directly exposed to TMA, leading to higher surface coverage. Because pre-deposition anneal primarily influences available nucleation sites rather than TMA adsorption mechanisms at these sites, AlO_x thickness and surface roughness remain largely constant.

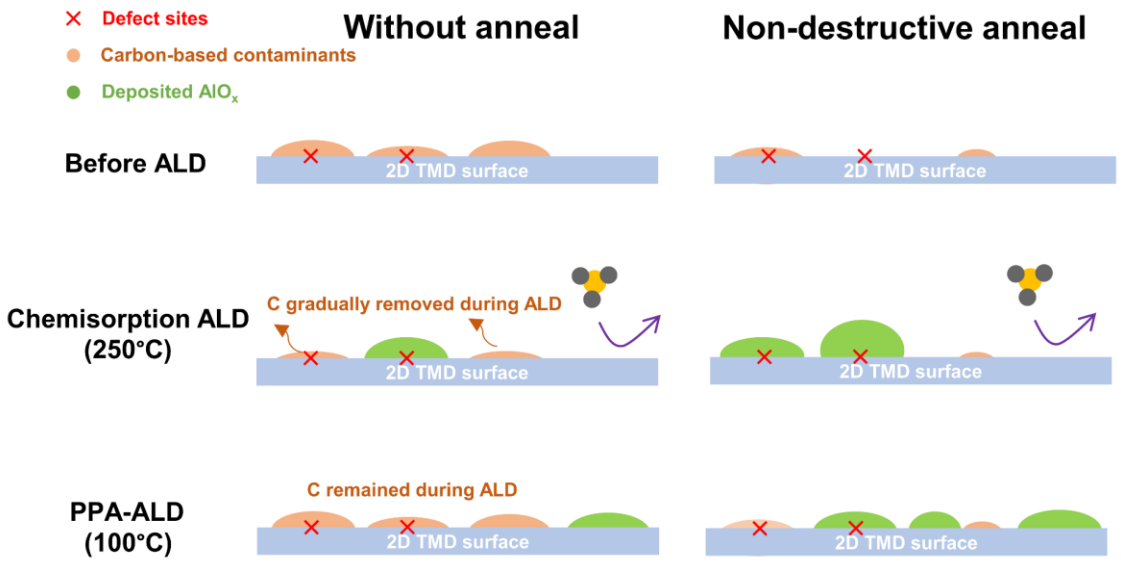

Figure 9. Schematic to explain the role of pre-deposition anneal on the AlO_x growth behavior for chemisorption-based and physisorbed-precursor-assisted (PPA) ALD.

We show the relationship between WCA of WS_2 monolayers and AlO_x surface coverage in Figure 10. Lower WCA can lead to higher surface coverage at identical ALD conditions. It should be noted that AlO_x surface coverage and WCA depend on the initial WS_2 morphology, which can vary significantly across different growth conditions and reactors. Nevertheless, the trend between WCA and dielectric surface coverage should remain consistent due to surface energy considerations. The result also indicates that fair comparisons between ALD-based dielectric deposition processes on 2D TMDs require similar initial surface conditions. We propose using water contact angle as an easy-to-obtain metric for assessing the 2D TMD surface conditions prior to ALD-based dielectric deposition.

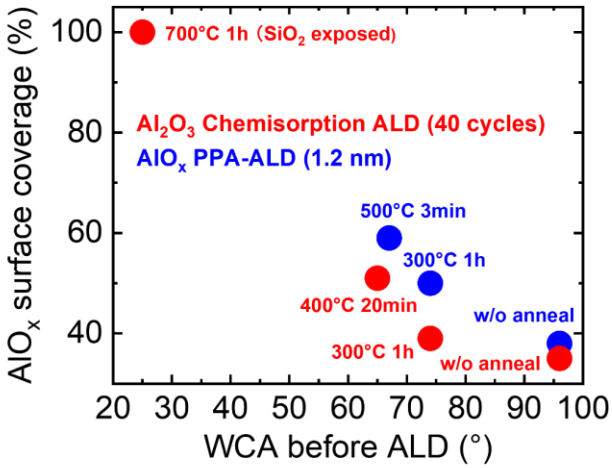

Figure 10. Relationship between AlO_x surface coverage and water contact angle obtained after pre-deposition anneals at various conditions.

IV. CONCLUSIONS and PERSPECTIVE

This study investigates how thermal annealing affects surface properties and ALD-based dielectric deposition on an MOCVD-grown WS_2 monolayer on a SiO_2/Si substrate. The WS_2 monolayer on SiO_2 remains stable under vacuum at temperatures up to 400°C for 1 hour. XPS measurements confirm that the lower water contact angle (WCA) after annealing at temperatures below 400°C results from the removal of surface carbon-based contaminants. The low WCA (~ 65°) persists only for a few hours after annealing, gradually saturating to ~ 90° over two weeks due to re-adsorption of contaminants. WS_2 exhibits a higher affinity for adsorbing airborne carbon-based contaminants compared to WO_x and SiO_2 surfaces. This may be attributed to the higher dispersive surface energy of the WS_2 monolayer as compared to the WO_x and SiO_2 surfaces. We investigate both conventional chemisorption-based and physisorbed-precursor-assisted (PPA) Al_2O_3 ALD on a WS_2 monolayer under various annealing

conditions. The observed growth behavior can be consistently explained by considering the changes of surface carbon-based contaminants. Our findings reveal a correlation between the WCA of a WS_2 monolayer and the surface coverage of subsequently deposited ALD-based dielectrics. This finding highlights the importance of surface pretreatment for ALD-based dielectric deposition on 2D TMDs.

In addition, pre-deposition anneal proves to enhance the surface coverage without increasing dielectric thickness in Al_2O_3 PPA-ALD, offering potential for further equivalent-oxide-thickness (EOT) scaling. We have demonstrated a 1.7-nm-thick pinhole-free AlO_x film using 5 cycles of PPA-ALD on a WS_2 monolayer[32]. Incorporating a pre-deposition anneal is expected to further enhance yield through increased surface coverage and potentially improve carrier transport due to reduced interface carbon. Furthermore, this technique may enable the realization of thinner continuous AlO_x layers with fewer PPA-ALD cycles or enable the integration of higher-κ dielectrics beyond Al_2O_3. Also, pre-deposition anneal can be also readily applied to complex 2D TMD structures, such as suspended nanosheets, where the fluid-structure interaction during wet chemical cleaning processes can be a concern.

Funding Sources

This work was done in the imec IIAP core CMOS programs and received funding from the European Union's Graphene Flagship grant agreement No 952792, 2D-EPL.

AUTHOR DECLARATIONS

Conflicts of Interest

The authors have no conflicts to disclose.

DATA AVAILABILITY

The data that support the findings of this study are available from the corresponding authors upon reasonable request.

REFERENCES

[1]D. Akinwande, C. Huyghebaert, C.-H. Wang, M. I. Serna, S. Goossens, L.-J. Li, H.-S. P. Wong, and F. H. L. Koppens, Nature **573**, 507 (2019).
[2]S.-K. Su, E. Chen, T. Y. T. Hung, M.-Z. Li, G. Pitner, C.-C. Cheng, H. Wang, J. Cai, H.-S. P. Wong, and I. P. Radu, in IEEE Symposium on VLSI Technology and Circuits (2022).
[3]M. Meuris, S. Arnauts, I. Cornelissen, K. Kenis, M. Lux, S. Degendt, P. Mertens, I. Teerlinck, R. Vos, L. Loewenstein, M. M. Heyns, and K. Wolke, in IEEE International Symposium on Semiconductor Manufacturing Conference Proceedings (1999).
[4]T. F. Schranghamer, M. Sharma, R. Singh, and S. Das, Chem. Soc. Rev. **50**, 11032 (2021).
[5]T. Li, W. Guo, L. Ma, W. Li, Z. Yu, Z. Han, S. Gao, L. Liu, D. Fan, Z. Wang, Y. Yang, W. Lin, Z. Luo, X. Chen, N. Dai, X. Tu, D. Pan, Y. Yao, P. Wang, Y. Nie, J. Wang, Y. Shi, and X. Wang, Nature Nanotechnology **16**, 1201 (2021).
[6]Y. Wan, J.-H. Fu, C.-P. Chuu, V. Tung, Y. Shi, and L.-J. Li, Chem. Soc. Rev. **51**, 803 (2022).
[7]F. Zhang, C. Erb, L. Runkle, X. Zhang, and N. Alem, Nanotechnology **29**, 025602 (2017).
[8]X. Li, Y. Zhu, W. Cai, M. Borysiak, B. Han, D. Chen, R. D. Piner, L. Colombo, and R. S. Ruoff, Nano Lett. **9**, 4359 (2009).
[9]A. Pirkle, J. Chan, A. Venugopal, D. Hinojos, C. Magnuson, S. McDonnell, L. Colombo, E. Vogel, R. Ruoff, and R. Wallace, Appl. Phys. Lett. **99**, 122108 (2011).
[10]Y.-Y. Chung, M.-L. Tsai, Y.-T. Ho, Y.-C. Tseng, and C.-H. Chien, ECS J. Solid State Sci. Technol. **7**, N46 (2018).
[11]W. H. Chang, N. Okada, M. Horikawa, T. Endo, Y. Miyata, and T. Irisawa, Jpn. J. Appl. Phys. **60**, SBBH03 (2021).
[12]M.-Y. Li, C.-H. Hsu, S.-W. Shen, A.-S. Chou, Y. C. Lin, C.-P. Chuu, N. Yang, S.-A. Chou, L.-Y. Huang, C.-C. Cheng, W.-Y. Woon, S. Liao, C.-I. Wu, L.-J. Li, I. Radu, H.-S. P. Wong, and H. Wang, in IEEE Symposium on VLSI Technology and Circuits (2022).
[13]M. Nakatani, S. Fukamachi, P. Solís-Fernández, S. Honda, K. Kawahara, Y. Tsuji, Y. Sumiya, M. Kuroki, K. Li, Q. Liu, Y.-C. Lin, A. Uchida, S. Oyama, H. G. Ji, K. Okada, K. Suenaga, Y. Kawano, K. Yoshizawa, A. Yasui, and H. Ago, Nature Electronics **7**, 119 (2024).
[14]D. Marinov, J.-F. de Marneffe, Q. Smets, G. Arutchelvan, K. M. Bal, E. Voronina, T. Rakhimova, Y. Mankelevich, S. El Kazzi, A. Nalin Mehta, P.-J. Wyndaele, M. H. Heyne, J. Zhang, P. C. With, S. Banerjee, E. C. Neyts, I. Asselberghs, D. Lin, and S. De Gendt, Npj 2D Mater Appl **5**, 17 (2021).

[15]M. Seol, M.-H. Lee, H. Kim, K. W. Shin, Y. Cho, I. Jeon, M. Jeong, H.-I. Lee, J. Park, and H.-J. Shin, Adv. Mater. **32**, 2003542 (2020).
[16]I. Asselberghs, T. Schram, Q. Smets, B. Groven, S. Brems, A. Phommahaxay, D. Cott, E. Dupuy, D. Radisic, J.-F. de Marneffe, A. Thiam, W. Li, K. Devriendt, A. Gaur, T. Maurice, D. Lin, P. Morin, and I. P. Radu, in IEEE Silicon Nanoelectronics Workshop (SNW) (2020)
[17]J. Kwon, M. Seol, J. Yoo, H. Ryu, D.-S. Ko, M.-H. Lee, E. K. Lee, M. S. Yoo, G.-H. Lee, H.-J. Shin, J. Kim, and K.-E. Byun, Nature Electronics **7**, 356 (2024).
[18]Q. Smets, T. Schram, D. Verreck, D. Cott, B. Groven, Z. Ahmed, B. Kaczer, J. Mitard, X. Wu, S. Kundu, H. Mertens, D. Radisic, A. Thiam, W. Li, E. Dupuy, Z. Tao, K. Vandersmissen, T. Maurice, H. C. Lin, and I. Radu, in IEEE International Electron Devices Meeting (IEDM) (2021).
[19]K. S. Kim, D. Lee, C. S. Chang, S. Seo, Y. Hu, S. Cha, H. Kim, J. Shin, J.-H. Lee, S. Lee, J. S. Kim, K. H. Kim, J. M. Suh, Y. Meng, B.-I. Park, J.-H. Lee, H.-S. Park, H. S. Kum, M.-H. Jo, G. Y. Yeom, K. Cho, J.-H. Park, S.-H. Bae, and J. Kim, Nature **614**, 88 (2023).
[20]R. Tilmann, C. Bartlam, O. Hartwig, B. Tywoniuk, N. Dominik, C. P. Cullen, L. Peters, T. Stimpel-Lindner, N. McEvoy, and G. S. Duesberg, ACS Nano **17**, 10617 (2023).
[21]K. P. O'Brien, C. J. Dorow, A. Penumatcha, K. Maxey, S. Lee, C. H. Naylor, A. Hsiao, B. Holybee, C. Rogan, D. Adams, T. Tronic, S. Ma, A. Oni, A. S. Gupta, R. Bristol, S. Clendenning, M. Metz, and U. Avci, in IEEE International Electron Devices Meeting (IEDM) (2021).
[22]Z. Li, Y. Wang, A. Kozbial, G. Shenoy, F. Zhou, R. McGinley, P. Ireland, B. Morganstein, A. Kunkel, S. P. Surwade, L. Li, and H. Liu, Nature Mater **12**, 925 (2013).
[23]K. Nagashio, Semicond. Sci. Technol. **35**, 103003 (2020).
[24]A.-S. Chou, T. Wu, C.-C. Cheng, S.-S. Zhan, I.-C. Ni, S.-Y. Wang, Y.-C. Chang, S.-L. Liew, E. Chen, W.-H. Chang, C.-I. Wu, J. Cai, H.-S. P. Wong, and H. Wang, in IEEE International Electron Devices Meeting (IEDM) (2021)
[25]S. McDonnell, B. Brennan, A. Azcatl, N. Lu, H. Dong, C. Buie, J. Kim, C. L. Hinkle, M. J. Kim, and R. M. Wallace, ACS Nano **7**, 10354 (2013).
[26]H. Liu, K. Xu, X. Zhang, and P. D. Ye, Appl. Phys. Lett. **100**, 152115 (2012).
[27]Y. Xu, T. Liu, K. Liu, Y. Zhao, L. Liu, P. Li, A. Nie, L. Liu, J. Yu, X. Feng, F. Zhuge, H. Li, X. Wang, and T. Zhai, Nature Mater **22**, 1078 (2023).
[28]H. Uchiyama, K. Maruyama, E. Chen, T. Nishimura, and K. Nagashio, Small, 2207394 (2023).
[29]S. J. McDonnell and R. M. Wallace, JOM **71**, 224 (2019).
[30]T. Knobloch, Y. Yu. Illarionov, F. Ducry, C. Schleich, S. Wachter, K. Watanabe, T. Taniguchi, T. Mueller, M. Waltl, M. Lanza, M. I. Vexler, M. Luisier, and T. Grasser, Nature Electronics **4**, 98 (2021).
[31]Y. C. Lin, C.-M. Lin, H.-Y. Chen, S. Vaziri, X. Bao, W.-Y. Woon, H. Wang, and S. S. Liao, IEEE Trans. Electron Devices **70**, 1454 (2023)
[32]Z. Lin, X. Wu, D. Cott, Y. Shi, H. Medina Silva, S. Sergeant, T. Conard, J. Meersschaut, A. Nalin Mehta, B. Groven, P. Morin, I. Asselberghs, C. J. Lockhart de la Rosa, G. S. Kar, D. Lin, and A. Delabie, ACS Appl. Electron. Mater. **6**, 4213 (2024).
[33]A. Kozbial, X. Gong, H. Liu, and L. Li, Langmuir **31**, 8429 (2015).

[34]P. K. Chow, E. Singh, B. C. Viana, J. Gao, J. Luo, J. Li, Z. Lin, A. L. Elías, Y. Shi, Z. Wang, M. Terrones, and N. Koratkar, ACS Nano **9**, 3023 (2015).
[35]H. Zhang, G. Arutchelvan, J. Meersschaut, A. Gaur, T. Conard, H. Bender, D. Lin, I. Asselberghs, M. Heyns, I. Radu, W. Vandervorst, and A. Delabie, Chem. Mater. **29**, 6772 (2017).
[36]W. Li, J. Zhou, S. Cai, Z. Yu, J. Zhang, N. Fang, T. Li, Y. Wu, T. Chen, X. Xie, H. Ma, K. Yan, N. Dai, X. Wu, H. Zhao, Z. Wang, D. He, L. Pan, Y. Shi, P. Wang, W. Chen, K. Nagashio, X. Duan, and X. Wang, Nature Electronics **2**, 563 (2019).
[37]M. Caymax, S. E. Kazzi, and C. Huyghebaert, in International Conference on Solid State Devices and Materials (2019).
[38]Y. Shi, B. Groven, Q. Smets, S. Sutar, S. Banerjee, H. Medina, X. Wu, C. Huyghebaert, S. Brems, D. Lin, P. Morin, M. Caymax, I. Asselberghs, and I. Radu, in IEEE International Electron Devices Meeting (IEDM) (2021)
[39]J. C. Kotsakidis, Q. Zhang, A. L. Vazquez de Parga, M. Currie, K. Helmerson, D. K. Gaskill, and M. S. Fuhrer, Nano Lett. **19**, 5205 (2019).
[40]S.-J. Jeong, H. W. Kim, J. Heo, M.-H. Lee, H. J. Song, J. Ku, Y. Lee, Y. Cho, W. Jeon, H. Suh, S. Hwang, and S. Park, 2D Mater. **3**, 035027 (2016).
[41]K. Kenis, P. W. Mertens, E. Altamirano-Sanchez, J. Van Ongeval, and M. De Vita, Solid State Phenom. **346**, 183 (2023).
[42]M. Annamalai, K. Gopinadhan, S. A. Han, S. Saha, H. J. Park, E. B. Cho, B. Kumar, A. Patra, S.-W. Kim, and T. Venkatesan, Nanoscale **8**, 5764 (2016).
[43]A. Berkdemir, H. R. Gutiérrez, A. R. Botello-Méndez, N. Perea-López, A. L. Elías, C.-I. Chia, B. Wang, V. H. Crespi, F. López-Urías, J.-C. Charlier, H. Terrones, and M. Terrones, Sci. Rep. **3**, 1755 (2013).
[44]J. Pető, T. Ollár, P. Vancsó, Z. I. Popov, G. Z. Magda, G. Dobrik, C. Hwang, P. B. Sorokin, and L. Tapasztó, Nature Chem **10**, 1246 (2018).
[45]Q. Liang, Q. Zhang, X. Zhao, M. Liu, and A. T. S. Wee, ACS Nano **15**, 2165 (2021).
[46]S. Li, T. Nishimura, M. Maruyama, S. Okada, and K. Nagashio, Nanoscale Adv. **5**, 405 (2023).
[47]T. R. Gengenbach, G. H. Major, M. R. Linford, and C. D. Easton, J. Vac. Sci. Technol. A **39**, 013204 (2021).
[48]H. Zhang, D. Chiappe, J. Meersschaut, T. Conard, A. Franquet, T. Nuytten, M. Mannarino, I. Radu, W. Vandervorst, and A. Delabie, J. Chem. Phys. **146**, 052810 (2016).
[49]G. N. Parsons, J. Vac. Sci. Technol. A **37**, 020911 (2019).